


Article

Effect of Current Density on the Performance of Ni–P–ZrO₂–CeO₂ Composite Coatings Prepared by Jet-Electrodeposition

Zhaoyang Song ¹, Hongwen Zhang ², Xiuqing Fu ^{1,3,*}, Jinran Lin ¹, Moqi Shen ¹, Qingqing Wang ¹ and Shuanglu Duan ¹

¹ College of Engineering, Nanjing Agricultural University, Nanjing 210031, China; 2019812053@njau.edu.cn (Z.S.); linjinran@njau.edu.cn (J.L.); 2017112001@njau.edu.cn (M.S.); 2018812044@njau.edu.cn (Q.W.); 33116524@njau.edu.cn (S.D.)

² College of Mechanical and Electrical Engineering, Shihezi University, Shihezi 832003, China; zhw_mac@shzu.edu.cn

³ Key laboratory of Intelligence Agricultural Equipment of Jiangsu Province, Nanjing 210031, China

* Correspondence: fuxiuqing@njau.edu.cn; Tel.: +86-139-1387-8179

Received: 4 May 2020; Accepted: 26 June 2020; Published: 29 June 2020



Abstract: The objective of this study was to improve the surface properties, hardness, wear resistance and electrochemical corrosion resistance of #45 steel. To this end, Ni–P–ZrO₂–CeO₂ composite coatings were prepared on the surface of #45 steel using the jet-electrodeposition technique by varying the current density from 20 to 60 A/dm². The effect of current density on the performance of the composite coatings was evaluated. Scanning electron microscopy (SEM), energy dispersive X-ray spectroscopy (EDS) and X-ray diffraction (XRD) were applied to explore the surface topography, elemental composition, hardness and electrochemical corrosion resistance of the composite coatings. The results showed that with the increase in the current density, the hardness, wear resistance, and electrochemical corrosion resistance tends to increase first and then decrease. At a current density of 40 A/dm², the hardness reached a maximum of 688.9 HV_{0.1}, the corrosion current reached a minimum of 8.2501×10^{-5} A·cm⁻², and the corrosion potential reached a maximum of −0.45957 V. At these values, the performance of the composite coatings was optimal.

Keywords: ZrO₂ nanoparticles; CeO₂ nanoparticles; composite coatings; jet-electrodeposition; current density

1. Introduction

In industrial production, the service life of a workpiece is an important indicator of its durability [1,2]. To improve the surface performance and service life of workpieces, researchers have applied surface treatment technologies to prepare composite coatings [3,4]. Ding et al. prepared Ni–graphene composite coatings on the surface of #45 steel using the brush plating technology. They obtained an extremely small grain size and excellent wear resistance and electrochemical corrosion resistance compared to Ni coatings [5].

ZrO₂ nanoparticles are inorganic, nonmetallic materials with excellent physical and chemical properties. Because of their high melting point, high boiling point, high hardness, excellent thermal stability and good corrosion resistance, they are widely used in fields such as materials, machinery and ceramics. CeO₂ nanoparticles are important rare earth materials owing to their excellent electrical and optical properties and single-crystal structure. They can suppress lattice growth and improve the surface quality of coatings [6–8]. Adding ZrO₂ or CeO₂ nanoparticles to a plating solution can significantly improve the wear and corrosion resistances of composite coatings [9,10].

Laszczynska et al. added ZrO₂ nanoparticles to a plating solution to improve the wear resistance of Ni–P alloy coatings, and prepared Ni–Mo–ZrO₂ composite coatings by electrodeposition. The addition of ZrO₂ nanoparticles significantly improved the hardness, wear resistance and adhesion of the composite coating [11]. Li et al. added CeO₂ particles with a particle size of 10 nm to prepare Ni–CeO₂ nanocomposite coatings. The CeO₂ nanoparticles inhibited the diffusion of Ni ions along the grain boundaries, thereby significantly enhancing the hardness and wear resistance of the Ni–CeO₂ nanocomposite coatings [12].

Codepositing ZrO₂ and CeO₂ nanoparticles can help take advantage of the composite synergy effect of multiple nanoparticles. Composite coatings with excellent properties can be obtained owing to the dispersion strengthening and pinning effect between different nanoparticles [13]. In the present study, a single nanoparticle composite coating was prepared using a surface treatment technology, and the results were compared with those of a pure substrate [14]. The composite synergy effect of multiple nanoparticles has rarely been studied, with even fewer studies on the effects of current density on the performance of composite coatings with multiple nanoparticles. In this context, Ni–P–ZrO₂–CeO₂ composite coatings were prepared by jet-electrodeposition to investigate the effects of current density on the surface morphology and properties of the coatings. The wear and corrosion resistances of the composite coatings were also analyzed.

2. Materials and Methods

2.1. Experimental

In this study, #45 steel was used as the base metal with a sample size of 25 mm × 10 mm × 8 mm. The sample surface was polished successively by no. 320, no. 800, no. 1500 and no. 2000 wet-and-dry sandpapers until it was reflective. The roughness value of the workpiece after the polishing treatment was determined using the Olympus LEXT 4100 laser confocal microscope: the surface roughness S_a was 0.012 µm, and the line roughness R_a was 0.149 µm. The sample was then placed in alcohol and ultrasonically cleaned. Table 1 lists the composition and content of the plating solution [15]. The pH of the plating solution was in the range of 1.0–1.5, and the temperature was 70 °C. Prior to jet-electrodeposition, preprocessing steps were applied to the workpiece: Oil removal → weak activation → strong activation, including rinsing with deionized water after each step. ZrO₂ and CeO₂ nanoparticles were purchased from Shanghai Yaotian New Material Technology Co., Ltd. (Shanghai, China). The sizes of the ZrO₂ and CeO₂ nanoparticles used in the experiment were 50 and 100 nm, respectively. Ni–P–ZrO₂–CeO₂ composite coatings were prepared by varying the current density from 20 to 60 A/dm². The preparation time of the coatings was 20 min. Finally, the processed workpieces were ultrasonically cleaned and air-dried.

Table 1. Composition of plating solution.

Composition	Content/(g·L ⁻¹)	Effect
NiSO ₄ ·6H ₂ O	200	Provide Ni ²⁺
NiCl ₂ ·6H ₂ O	30	Reduce free cations
H ₃ PO ₃	20	Provide P
H ₃ BO ₃	30	pH SRP
C ₆ H ₈ O ₇	60	Buffer, complexing agent
CH ₄ N ₂ S	0.01	Stabilizer
C ₁₂ H ₂₅ SO ₄ Na	0.08	Surfactant
ZrO ₂ nanoparticles (50 nm)	10	Secondary phase nanoparticles
CeO ₂ nanoparticles (100 nm)	1	Secondary phase nanoparticles

Figure 1 shows the experimental schematic of the jet-electrodeposition process. As shown, the workpiece clamped by clamping tool 2 was connected to the cathode of the DC power source for the reduction reaction, and nickel rod 6 was connected to the anode of the DC power source for the oxidation reaction. Nozzle 5 with nickel rod was installed on the spindle of machine tool 7 to realize a reciprocating movement during the deposition. Plating solution 3 was pumped from reservoir 10 to the nozzle by pump 9 and was sprayed to the surface of the workpiece, thus completing the jet-electrodeposition process. The sprayed plating solution was returned to the reservoir through catheter 8 for collection and reuse, which improved the overall efficiency. After the power was turned on, the nickel rod, plating solution, and workpiece form a closed loop to realize the deposition of ions.

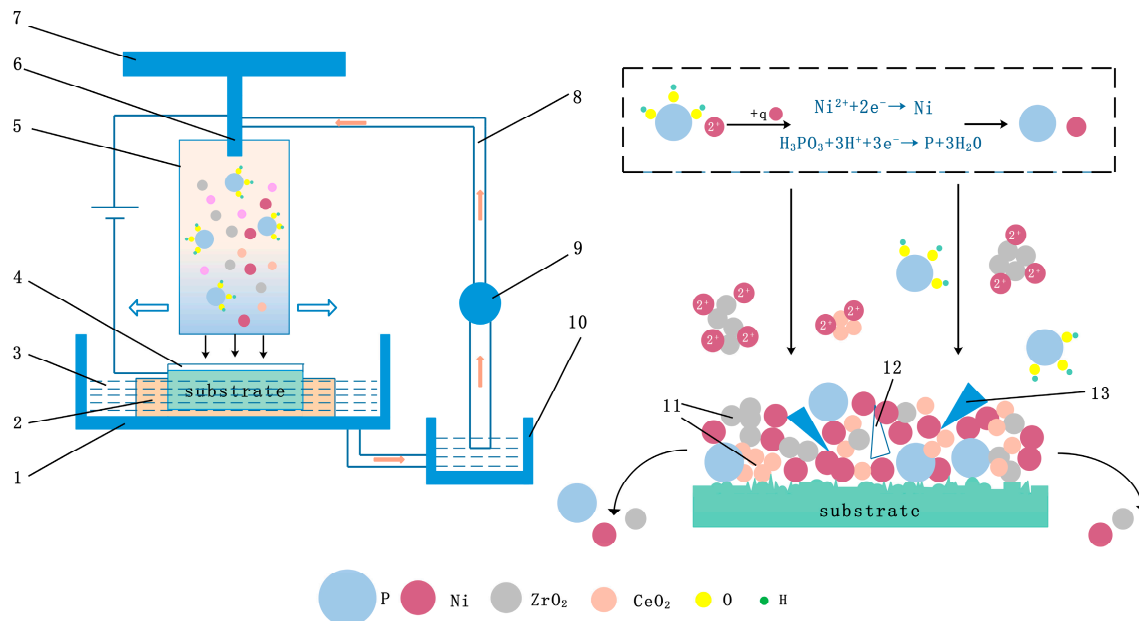


Figure 1. Experimental schematic of jet-electrodeposition. 1—seal groove; 2—clamping tool; 3—plating solution; 4—coating; 5—nozzle; 6—nickel rod; 7—machine tool spindle; 8—catheter; 9—sinking pump; 10—reservoir; 11—agglomeration phenomenon; 12—hump 13—pit.

The plating solution contained a significant amount of Ni and P ions and ZrO₂ and CeO₂ nanoparticles. Under the action of an electric field, Ni²⁺ and H₃PO₃ gain electrons and form Ni and P atoms, which were then evenly deposited on the surface of the workpiece during high-speed injection. The ZrO₂ and CeO₂ nanoparticles appeared to have agglomerated because of their high surface energy [16]. A significant amount of ZrO₂ and CeO₂ nanoparticles heaped up individually and with each other. Based on the Guglielmi adsorption mechanism [17], ZrO₂ and CeO₂ nanoparticles attract and adhere to Ni²⁺ and then codeposit on the surface of the substrate. The nanoparticles hinder the “tip effect” [18] of the nickel-based metal phases. Moreover, they promote each other’s deposition and give full play to the characteristics of the synergetic growth with each other. Therefore, the two types of nanoparticles were evenly distributed, further improving the surface quality of the composite coatings.

2.2. Instruments

A Quanta FEG 250 field-emission scanning electron microscope (FE-SEM) from FEI Instruments, Inc. (Hillsboro, OR, USA) was used to investigate the microscopic surface morphology of the composite coatings at an accelerating voltage of 15 kV and a scan rate of 30 μs. An energy dispersive X-ray spectroscope (EDS) from Bruker AXS, Inc. (Berlin, Germany) was used to investigate the elements and their contents in the composite coatings. The accelerating voltage was 16 kV, working distance was 11 mm; the scan area was 1 mm². The phase structure of the composite coating was analyzed

using an X-ray diffractometer (PANalytical X'pert; PANalytical, Inc., Almelo, The Netherlands) at an operating voltage of 40 kV, scan rate of 5°/min and scanning range (2θ) of 20°–90°. The HighScore Plus software was used to analyze the XRD results. A hardness measurement instrument (Duramin-40; Struers, Inc., Copenhagen, Denmark) was used to determine the hardness. The microhardness was measured by maintaining a 100 g load for 15 s and the average of five replicates was taken as the final value. A CFT-I comprehensive property tester was used to mark the coating surface back and forth for 20 min, with a wear mark length of 4 mm and a load of 320 g. An Olympus LEXT 4100 laser confocal microscope (OLYMPUS, Tokyo, Japan) was used to measure the dimension parameters of the friction marks on the surface of the composite coatings. An electrochemical workstation (CS350, Wuhan CorrTest Instruments Corp., Ltd., Wuhan, China) was used to investigate the electrochemical corrosion experiments using a three-electrode-cell electrochemical test method. Under the open circuit potential, the potentiodynamic polarization curves of the coating were obtained using a potentiodynamic scanning method, and the impedance spectrum of the coating was tested using the alternating current impedance method. The corrosive medium was 35-g/L NaCl solution. The objective was to simulate the corrosion characteristics of the workpieces due to seawater solution and reflect the actual corrosion behavior as much as possible [19]. The working electrode was the electrochemical sample, the auxiliary electrode was Pt, and the reference electrode was a saturated calomel electrode. The workpiece sample was encapsulated with epoxy resin, leaving an exposed area of 1 cm², and then immersed in NaCl solution. The test frequency was in the range of 0.01–1 × 10⁵ Hz, and the scanning direction was from high frequency to low frequency.

3. Results and Discussion

3.1. Analysis of Micromorphology of the Composite Coating

3.1.1. Analysis of Surface Micromorphology of the Composite Coating

Figure 2 shows the surface micromorphologies of the Ni–P–ZrO₂–CeO₂ composite coatings obtained at different current densities. The morphology shows a typical cellular structure, the size of which varies with the current density. The main reason is the codeposition of the catalytic active center [20] on the surface of the coatings with Ni, P, etc., to form a solid solution. During the growth process, a cellular structure was formed, and its growth conformed to the 2D-crystal nuclei growth model [21]. When the current density is 20 A/dm², the cell structure of the composite coating is not obvious, the number of nanoparticles on the surface is small, and the surface of the coating is uneven. As shown, when the current density is increased from 20 to 40 A/dm², the surface quality of the composite coating is significantly improved, the coating is smoother, the cellular structure is smaller and more uniform, the amount of defects, such as pits, is significantly reduced, and the number of nanoparticles on the coating surface is increased and distributed uniformly. When the current density is 40 A/dm², it can be seen that there is obvious nanoparticle agglomeration on the surface. When the current density is increased from 40 to 60 A/dm², the surface of the composite coating is rougher, more pits and humps are observed, the number of nanoparticles decreases, the cellular structure is no longer uniform, and cracks appear.

The analysis results show that increasing the current density will directly lead to an increase in the deposition rate. Significant amounts of ZrO₂ and CeO₂ nanoparticles were surrounded by Ni²⁺ ions, which were deposited on the substrate surface. Under the action of strong and weak adsorption, the nucleation rate in the composite coating increased. Dispersion strengthening and fine-grain strengthening were realized through the composite synergy effect between the nanoparticles, thereby improving the surface quality of the coating. However, when the current density exceeded a certain value, electromigration controlled the transmission of the nickel ions, and ultrasonic forced convection controlled the transmission of the nanoparticles in the plating solution [22]. This reduced the deposition rate of the ZrO₂ and CeO₂ nanoparticles, resulting in fewer particles in the coating and a weakening of the dispersion strengthening and grain refinement effect of the particles. In addition,

an excess current density distorted the structure of the coatings, resulting in many dislocations and increased interior stress [23], which also directly caused many cracks on the surface. Moreover, the excess current density directly provided energy for the agglomeration of the particles on the surface of the coatings. Numerous uneven agglomerated blocks of nanoparticles were deposited on the surface, forming protrusions and resulting in a rough surface and poor surface quality.

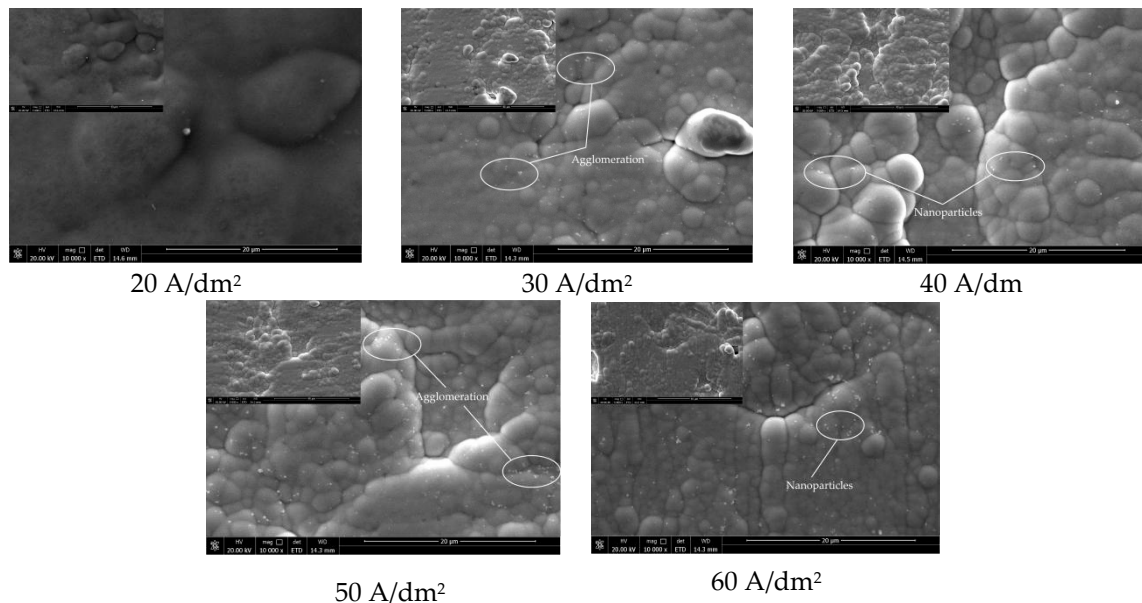


Figure 2. Surface micromorphologies of Ni-P-ZrO₂-CeO₂ composite coatings prepared at different current densities.

3.1.2. Analysis of Cross-Sectional Micromorphology of Composite Coating

Figure 3 shows the cross-sectional micromorphologies of the composite coating obtained by SEM. The thicknesses of the composite coatings with current densities of 20, 30, 40, 50 and 60 A/dm² are 11.7, 17.9, 23.2, 18.3 and 15.9 μ m, respectively. The thickness of the composite coating increases first and then decreases. When the current density is 40 A/dm², the thickest composite coating is 23.2- μ m-thick, which is 98% and 56% higher than those prepared at current densities of 20 and 60 A/dm², respectively. The composite coatings prepared at current densities of 20 and 60 A/dm² have holes and cracks. When the current density is 40 A/dm², the structure of the composite coating is dense, there are only a few defects, such as hole cracks, and the cross section of the composite coating is smooth and flat. With the increase in the number of ZrO₂ and CeO₂ nanoparticles deposited on the composite coating, the nanoparticles become evenly dispersed in the coating when the current density is 40 A/dm², thus better filling the internal gaps in the composite coating. Moreover, the increase in the number of nucleation particles is beneficial to improving the uniformity of the unit cell structure, making the plating layer dense. Excessive nanoparticles lead to evident agglomeration on the surface of the substrate. Therefore, the active sites on the substrate surface are covered and blocked by the agglomerated nanoparticles, and they lose their activity [24]. The number of nucleation sites is reduced, and the distribution of the internal force during growth is uneven, thus easily leading to cracks and other defects.

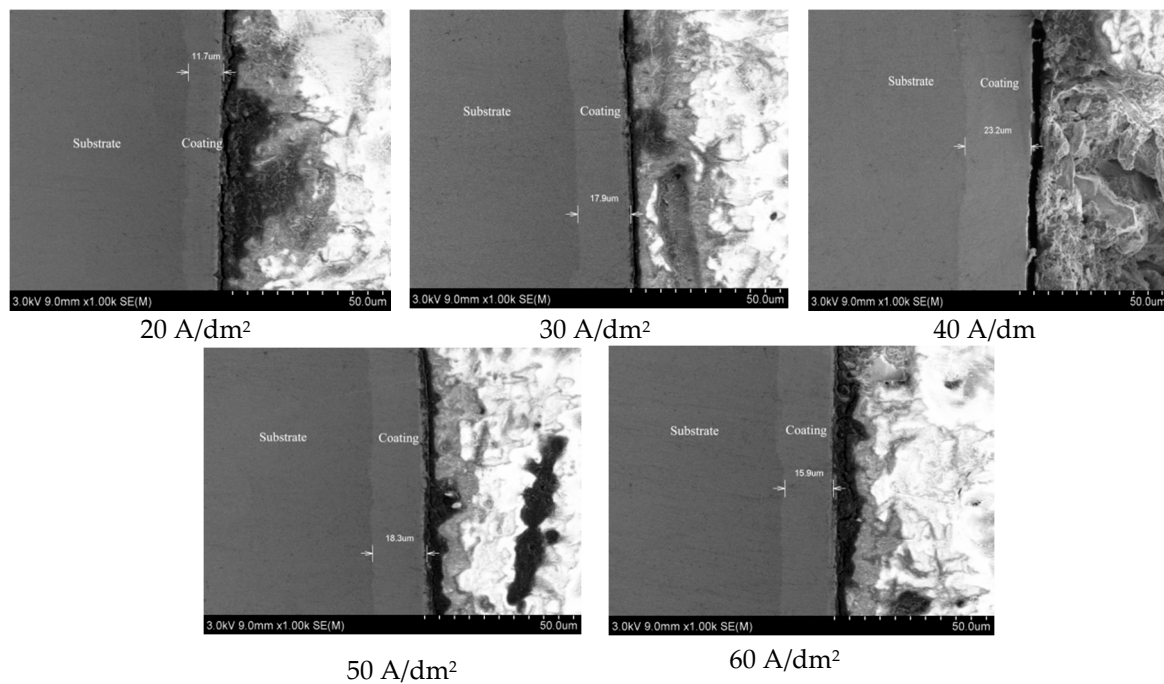


Figure 3. Cross-sectional micromorphologies of Ni-P-ZrO₂-CeO₂ composite coatings prepared at different current densities.

3.2. Effect of Current Density on Coating Composition

3.2.1. XRD Analysis of Composite Coating

Figure 4 shows the measured XRD spectra of the composite coatings under different current densities, including a comparison with the standard PDF card. Clearly, the grain growth directions of the coatings are the same. All the composite coatings exhibit strong diffraction peaks of Ni. The XRD peaks at $2\theta = 44.6^\circ$, 52.2° and 76.8° correspond to Ni (111), (200) and (220) crystal faces, respectively. The three main peaks are sharp at the top and wide at the bottom, indicating that the composite coating is composed of a mixture of crystalline and amorphous phases, all of which are face-centered cubic structures. Extremely small ZrO₂ diffraction peaks appear at $2\theta = 82.5^\circ$. No evident Ce peaks can be detected in the XRD patterns; this can be attributed to the fewer CeO₂ nanoparticles in the plating solution. Table 2 presents the relationship between the current density and the grain size of the Ni (111) crystal plane, calculated using the Scherrer formula [25]. The grain size of the Ni (111) crystal plane tends to decrease first and then increase with increasing current density. At a current density of 40 A/dm², the grain size reaches a minimum of 6.2 nm. At this time, the effect of grain refinement is the most evident. The grain size is reduced by 1.8 nm compared with that at a current density of 20 A/dm². The Jade 6 software was used to analyze and calculate the grain size and crystallinity. The ratio of the area of all the crystal peaks to the total area of all the diffraction peaks represents the crystallinity. The calculation formula is as follows:

$$\text{Crystallinity}(\%) = \frac{S_{\text{Crystal peak}}}{S_{\text{Total peak}}} \times 100\% \quad (1)$$

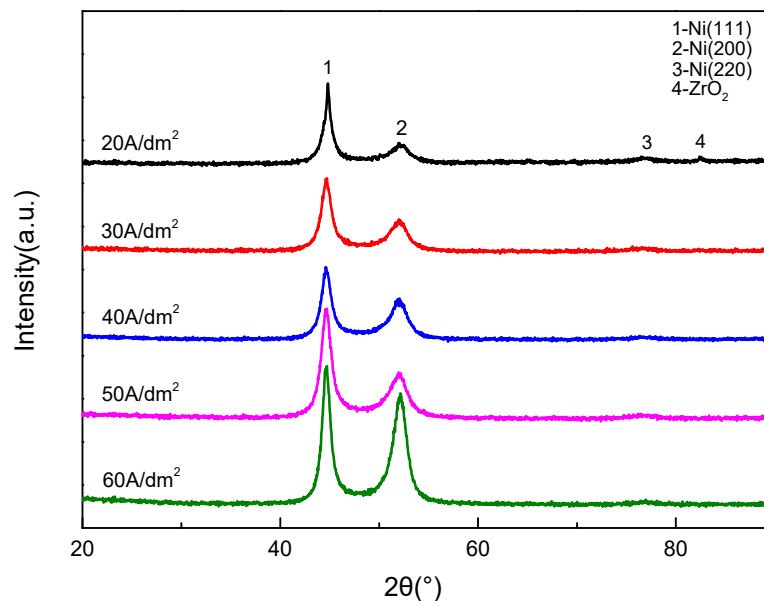


Figure 4. XRD patterns of Ni-P-ZrO₂-CeO₂ composite coatings prepared at different current densities.

Table 2. Relationship between current density and crystallinity and grain size of Ni (111) crystal surface.

Current Density (A/dm ²)	Grain Size (nm)	Crystallinity (%)
20	8.0	35.09
30	6.7	32.12
40	6.2	49.71
50	6.4	69.05
60	7.0	74.01

Based on the Guglielmi adsorption model, ZrO₂ and CeO₂ nanoparticles are embedded in the composite coating through strong and weak adsorption. As nucleation centers, the nanoparticles provided several nucleation growth points via the composite synergy effect, which increased the nucleation rate of the composite coating and promoted the formation of new grains and inhibited the growth of the formed grains. Moreover, the effect of grain refinement was evident, which avoided the excessive growth of only one type of nanoparticles. Therefore, the microstructure of the composite coating was more uniform, and the surface properties were improved. The current density had an important effect on the adsorption of the nanoparticles on the surface of the substrate, nucleation rate and crystal growth rate, which also directly affected the grain size. As the current density increased, the deposition rate of Ni increased, and the number of ZrO₂ and CeO₂ nanoparticles embedded in the composite coating increased, resulting in grain refinement. With increasing current density, the higher peak potential intensified the hydrogen evolution reaction of the cathode, which was not conducive to the deposition of the nanoparticles, and the grain refinement effect of the nanoparticles on the composite coating was also reduced.

3.2.2. EDS and Mass Fraction Analysis of Composite Coatings

Table 3 gives the mass fraction of each element on the surface of the composite coating. Under different current density conditions, the elements in the coating have a varying degree of influence. With increasing current density, the mass fraction of Ni decreases first and then increases. At a current density of 40 A/dm², the mass fraction is 85.81%. In addition, when the current density is 40 A/dm², the Zr and Ce contents in the composite coating are maximum: 3.79% and 10.36%, respectively. These results show that increasing the current density of the cathode would increase the overpotential and polarization of the cathode, which is conducive to the deposition of more ZrO₂

and CeO_2 nanoparticles, thus relatively increasing the mass fractions of Zr and Ce and relatively decreasing the mass fractions of Ni and P in the composite coating. As the current density continues to increase, the relative contents of Ni and P in the composite coating increase again because of the decrease in the number of ZrO_2 and CeO_2 nanoparticles. As rare earth elements and surface active elements, the Ce ions have a large effective charge number, can provide empty orbits, can accelerate the transfer and transmission of free electrons, have a strong adsorption capacity, and can be preferentially adsorbed on the substrate to form nucleus particles; therefore, its deposition rate is higher than those of other elements, and the mass fraction of elements deposited in the composite coating is relatively higher than those of the other elements. Figure 5 shows the content of each element in the composite coating. As shown, the coating contains Ni, P and Zr elements and weak Ce peaks in the energy spectra, demonstrating the successful preparation of the Ni-P-ZrO₂-CeO₂ composite coating by jet-electrodeposition. Conduct EDS surface distribution test when the current density is 40 A/dm², select the Ni, Ce, Zr elements in the composite coating for marking. The distribution map of each element of the composite coating and EDS spectrum is obtained. It can be seen from Figure 6 that each element is evenly distributed on the surface of the composite coating, and a small amount of Ce and Zr element distribution points appear on the surface.

Table 3. Mass fraction of elements on the coating surface at different current densities.

Current Density (A/dm ²)	Ni (wt%)	P (wt%)	Zr (wt%)	Ce (wt%)
20	90.13	1.16	3.74	4.98
30	88.64	0.40	4.67	6.29
40	85.81	0.04	3.79	10.36
50	90.17	0.93	2.39	6.51
60	90.08	1.13	3.68	5.11

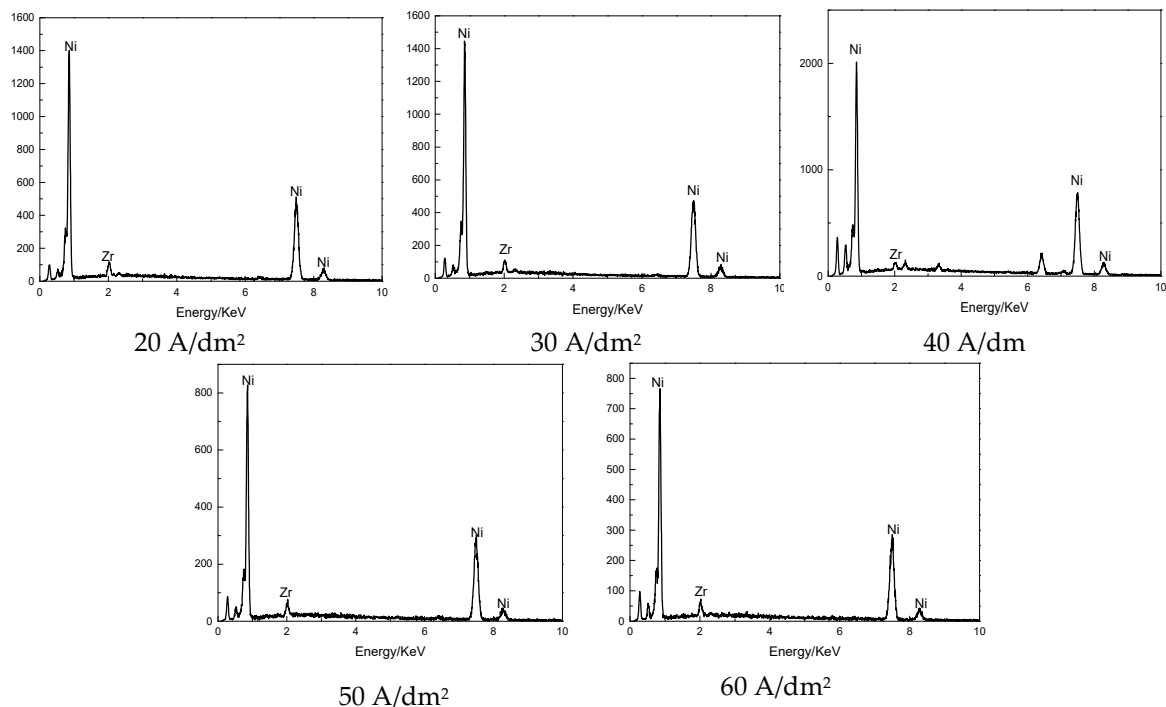


Figure 5. EDS spectra of Ni-P—ZrO₂-CeO₂ composite coatings prepared at different current densities.

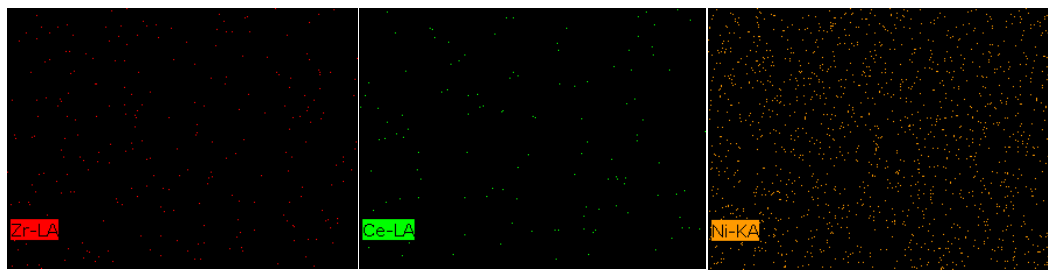


Figure 6. The distribution map of each element and EDS spectrum of the composite coating at the current density of 40 A/dm².

3.3. Effects of Current Density on Coating Hardness and Wear Resistance

3.3.1. Analysis of Microhardness of Composite Coating

Figure 7 shows the relationship between the hardness of the composite coating and the current density. The microhardness of the Ni–P–ZrO₂–CeO₂ composite coatings tends to increase first and then decrease with increasing current density. When the current density is increased from 20 to 40 A/dm², the microhardness increases from 596.4 HV_{0.1} to 688.9 HV_{0.1}. This was because the current density of the cathode directly affected the deposition rate of the particles in the composite coating. When the current density is relatively low, the electrostatic attraction of the cathode to the ZrO₂ and CeO₂ nanoparticles is relatively weak, and the ion deposition rate in the plating solution is low. This decreases the number of nanoparticles in the coating, resulting in a thin composite coating with low hardness. With increasing current density, under the effect of the electric field, the Ni²⁺ and ZrO₂ and CeO₂ nanoparticles accelerate the deposition, and the number of nanoparticles embedded in the composite coating increases. The nanoparticles serve as a reinforcing phase, dispersed in the composite coating, which effectively prevent the internal dislocation and grain boundary slip of the composite coating [26], thereby improving the hardness and wear resistance. When the current density is increased from 40 to 60 A/dm², the microhardness of the composite coating decreases from 688.9 to 659.9 HV_{0.1}. This was because the excessive current density made the reaction more violent, and the surface of the composite coating was constantly scoured, which was not conducive to the deposition of the particles. Moreover, the ZrO₂ and CeO₂ nanoparticles already deposited on the surface of the coating hindered the codeposition of Ni, P and nanoparticles to a certain extent, which reduced the number of nanoparticles in the composite coating, thus decreasing the hardness. At a current density of 40 A/dm², the hardness of the composite coatings reaches a maximum of 688.9 HV_{0.1}, which is approximately 12.5% higher than that when the current density is 20 A/dm². At this time, the composite coating exhibits a dense structure and the highest hardness value.

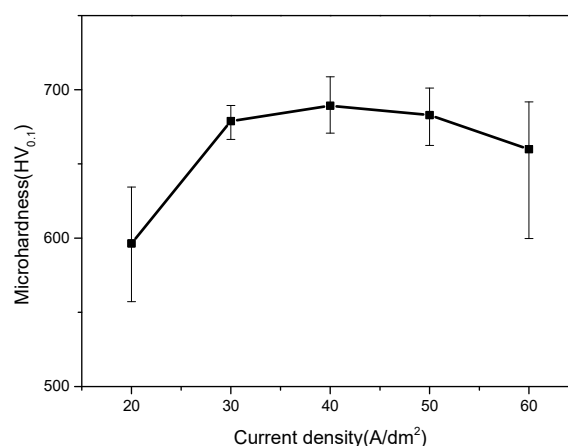


Figure 7. Relationship between microhardness of composite coatings and current density.

3.3.2. Wear Resistance Analysis of Composite Coating

Figure 8 and Table 4 present the cross-sectional morphologies and dimensional parameters of the wear scars of the composite coating under different current densities observed using the laser confocal microscope, respectively. Under the friction provided by the GCr15 grinding ball, the surface of the composite coating underwent plastic deformation and chemical bond interactions between the atoms, leading to cracks in the coating [27]. As shown, with increasing current density, the width, height and area of the wear scars first decrease and then increase. When the current density is increased from 20 to 40 A/dm², the degree of wear scar depression is gradually reduced, and the wear scars become shallower and thinner. When the current density is increased from 40 to 60 A/dm², the wear scars become more depressed and wider. At a current density of 40 A/dm², the degree of wear scar depression is low, the width reaches a minimum of 469.269 μm , and the height reaches a minimum of 8.757 μm . At this time, the wear resistance of the composite coating is the best.

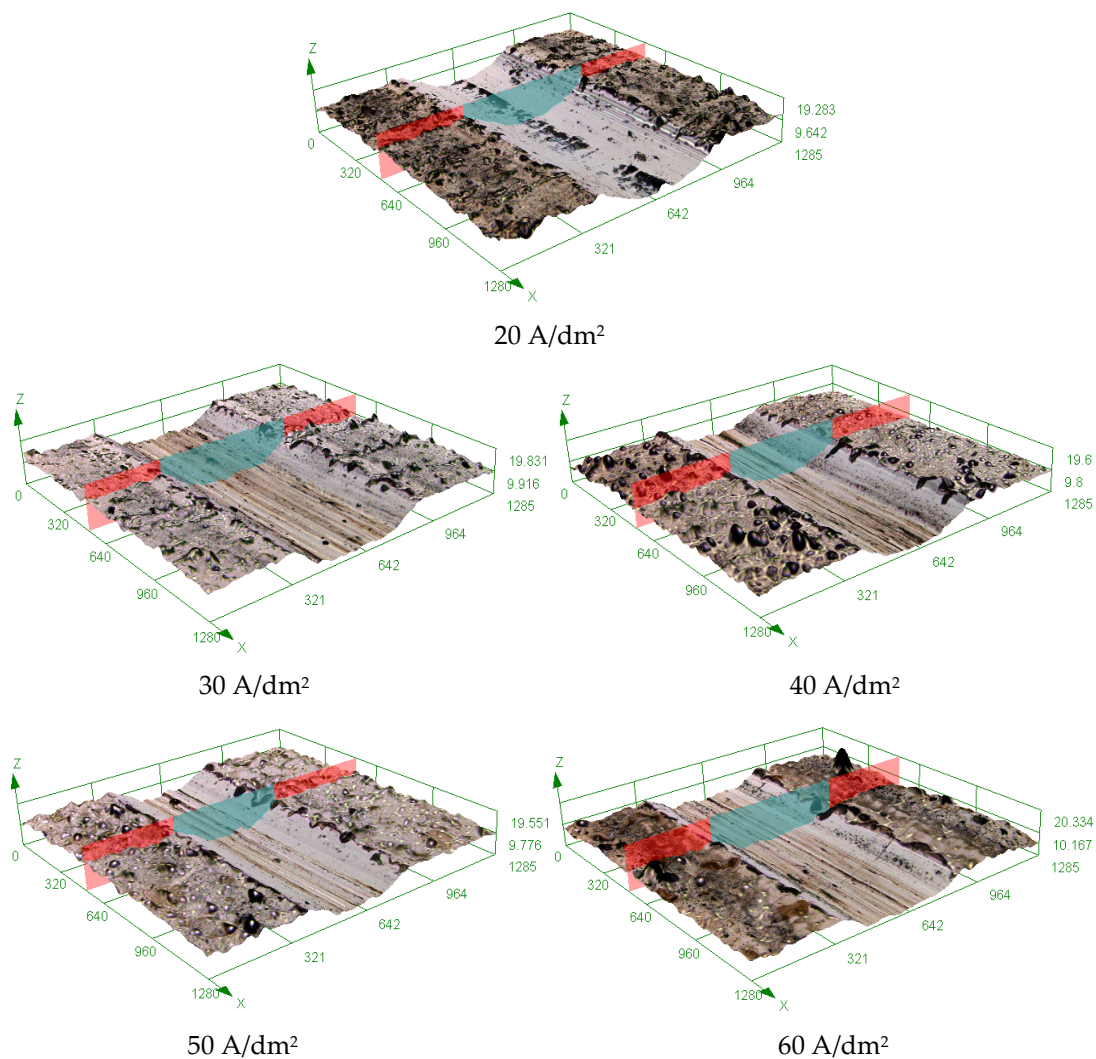


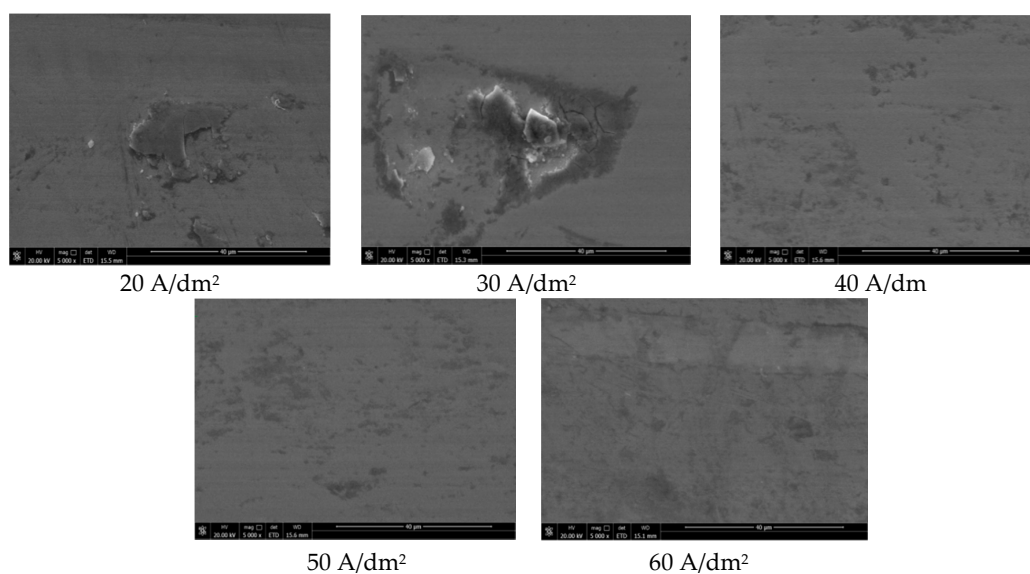
Figure 8. Cross-sectional morphologies of wear scars on composite coatings at different current densities.

Table 4. Section parameters of wear scars on composite coatings under different current densities.

Current Density (A/dm ²)	Width (μm)	Height (μm)	Scratch Area (μm ²)
20	568.011	10.629	3670.768
30	563.230	10.014	3519.558
40	469.269	8.757	2910.972
50	471.409	9.137	3045.194
60	512.349	8.941	3024.932

The analysis shows that, on one hand, according to the Archard theory [28], when the other conditions and parameters were consistent, the wear resistance of the composite coating was positively related to its hardness. The higher the hardness, the more wear resistant the composite coating. When the current density was low, a few ZrO₂ and CeO₂ nanoparticles were embedded in the composite coating, which weakened the fine-grain strengthening effect, resulting in a low hardness value and evident plastic deformation during friction. This also deteriorated the wear resistance. With increasing current density, an increasing number of ZrO₂ and CeO₂ nanoparticles surrounded by Ni²⁺ were deposited on the surface of the substrate. Their dispersion strengthening and pinning effect could effectively improve the hardness of the composite coating, and the microstructure had also changed, which enhanced their ability to resist plastic deformation. The wear resistance was also improved. On the other hand, nanoparticles were embedded in the composite coating as second phase solid particles. The high hardness of the nanoparticles helped improve the ability of the composite coating to resist the abrasive wear, which hindered the movement of the dislocations and enhanced the dispersion strengthening. The wear resistance of the composite coating was significantly improved owing to the combination of these two aspects.

Figure 9 shows the SEM analysis of the wear scars on the composite coating after surface friction. With the increase in the current density, the surface morphology of the Ni-P-ZrO₂-CeO₂ composite coating first exhibits a flattening trend and then a roughening one. When the current density is low, the wear of the composite coating is severe, the coating surface is softened by heat and many pits, furrows, bulges and peelings appear. The abraded surface is locally agglomerated. At this time, the wear type is mainly adhesive wear. With increasing current density, the degree of wear gradually decreases, the surface becomes smoother with fewer defects, and the wear morphology changes to abrasive wear [29]. With increasing current density, defects, such as pits, gradually appear on the surface.

**Figure 9.** SEM images of wear scars on composite coatings prepared at different current densities after friction tests.

The analysis results show that, on one hand, according to the Archard theory, the wear resistance of the composite coating is positively related to its hardness. As the current density increases, the pinning effect of the nanoparticles increases, and the hardness and wear resistance of the composite coating are significantly improved. The surface quality is improved after the friction test. With further increase in the current density, the hardness and wear resistance of the composite coating decrease, and the surface quality deteriorates after the friction test. This is consistent with the cross-section topography results of the wear scars. On the other hand, with the increase in the current density, more ZrO_2 and CeO_2 nanoparticles exhibited the “sliding balls” effect. To a certain extent, they made up for the pits and scratches left after the coating surface was damaged by abrasion [30]. Moreover, the nanoparticles formed a structure similar to a “protective film” on the friction surface, which had certain lubrication and supporting effects in that it avoided the direct contact between the friction balls and the surface of the composite coating, thereby improving the surface quality of the composite coating after the friction test. In addition, the ZrO_2 and CeO_2 nanoparticles had the effect of antiwear particles. As the current density increased, the pressure on the nanoparticles as antiwear particles decreased, which significantly reduced the adhesive wear of the composite coating [31]. As the current density continued to increase, the number of ZrO_2 and CeO_2 particles decreased and the lubrication effect decreased. Moreover, the particle distribution was uneven, and agglomeration occurred. The agglomerated nanoparticles exhibited a low binding force and high hardness and easily attached to the surface of the grinding balls to form hard “abrasive particles,” which further destroyed the composite coating and deteriorated the surface quality [32].

3.4. Effect of Current Density on Corrosion Resistance of Composite Coating

3.4.1. Corrosion-Resistance Polarization Curve of Composite Coating

CorrTest software and polarization curve epitaxy were used to obtain the polarization curves and parameter values of the corrosion resistance of the composite coatings under different current density conditions, as shown in Figure 10 and Table 5. The lower the corrosion current density and the higher the corrosion potential, the better the corrosion resistance [33]. At a current density of 20 A/dm^2 , the corrosion current reaches a maximum of $2.2038 \times 10^{-3} \text{ A}\cdot\text{cm}^{-2}$, and the corrosion potential reaches a minimum of -0.78842 V . At a current density of 40 A/dm^2 , the corrosion current reaches a minimum of $8.2501 \times 10^{-5} \text{ A}\cdot\text{cm}^{-2}$, and the corrosion potential reaches a maximum of -0.45957 V . The corrosion resistance is the best at that time. Compared with that at a current density of 20 A/dm^2 , the corrosion potential is increased by 42.3%, and the corrosion current is decreased by 96.08%. With the increase in the current density, the corrosion resistance tends to first increase and then decrease.

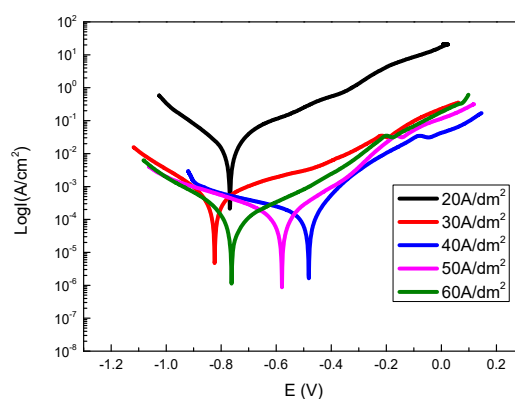


Figure 10. Polarization curves of corrosion resistance of composite coatings prepared at different current densities.

Table 5. Parameter values of polarization curve.

Current Density (A/dm ²)	E_{corr} (V)	I_{corr} (A·cm ⁻²)	B_a (mV)	B_c (mV)	Corrosion Rate (mm/a)
20	−0.78842	2.204×10^{-3}	205.81	231.52	192.75
30	−0.82373	7.879×10^{-4}	562.56	263.94	6.8915
40	−0.45957	8.251×10^{-5}	93.338	201.95	0.7215
50	−0.58009	1.609×10^{-4}	223.78	381.96	1.4074
60	−0.78762	2.704×10^{-4}	438.14	181.00	2.3651

The analysis results show that, during the corrosion process, the corrosion particles in the corrosion medium continuously invade and penetrate the composite coating through different paths, which form a corrosion cell with the grain boundary as the anode and the lattice as the cathode, so that the composite coating is randomly eroded from the grain boundary. With increasing current density, more ZrO₂ and CeO₂ nanoparticles were embedded in the composite coating. On one hand, the dispersed nanoparticles served as strengthening phases, which made the composite coating harder and the structure more detailed and compact. This also made it more difficult for the corrosive media to penetrate the coating or even the substrate and improved the chemical stability and corrosion resistance of the composite coating. On the other hand, the nanoparticles in the composite coating were preferentially corroded during the corrosion process, hindering the anode reaction of the coating corrosion process, thereby slowing down the corrosion reaction process. In addition, the nanoparticles formed a fine-grained “protective film” on the surface of the coating through the fine-grain strengthening effect [34], which retarded the corrosion process, reduced the corrosion rate and improved the corrosion resistance of the composite coating. When the current density continued to increase, the excess current density made the reaction more violent, suppressed the deposition of the nanoparticles and decreased the number of ZrO₂ and CeO₂ nanoparticles in the composite coating. As the strengthening phases, the nanoparticles weakened the fine-grain strengthening effect, inhibited the corrosion process and reduced the corrosion resistance of the composite coating. In this study, the polarization curve epitaxy method was used to determine the corrosion rate, and it can be directly calculated according to Faraday’s law [35]. In accordance with the polarization curve epitaxy method, the point in the positive direction of the polarization potential that deviates from the corrosion potential by 50 mV is recorded as point A the point in the negative direction of the polarization potential that deviates from the corrosion potential by 50 mV is recorded as point B. The Tafel constants at points A and B are b_A and b_B , respectively. Two straight lines are drawn, and their intersection point is determined. The corresponding current density at the intersection point is the corrosion current density, which can directly characterize the corrosion rate. According to the Stern–Geary equation:

$$i_{\text{corr}} = \frac{b_A \times b_B}{2.303R_p(b_A + b_B)} \quad (2)$$

where b_A and b_B are the slopes of the anode and cathode dynamic potential polarization curves, respectively; R_p is the equivalent linear polarization resistance; i_{corr} is the corrosion current density. According to Faraday’s law, the corrosion depth can be obtained from the corrosion current density and the corrosion depth is used to characterize the corrosion rate V (mm/a).

$$V(\text{mm/a}) = \frac{3.27i_{\text{corr}}A}{nD} \times 10^{-3} \quad (3)$$

where A is the atomic weight of the metal; n is the number of gained or lost electrons; D is the density of the metal material.

3.4.2. Corrosion-Resistance Impedance Curve of Composite Coating

The CorrTest software was used to conduct the AC impedance test. Figure 11 and Table 6 present the equivalent circuit diagram, Nyquist diagram and equivalent circuit parameter values after fitting. In Figure 11, R_s is the resistance of the plating solution, R_p is the charge transfer resistance and CPE is the constant phase angle element. In the AC impedance spectrum, the capacitive arc radius has a certain relationship with the corrosion resistance of the composite coating. The higher the capacitive arc radius, the higher the resistance of charge conduction and the better the corrosion resistance of the coating [36]. Figure 11 shows that all lines are arc-shaped, indicating that all the coatings exhibit the characteristics of the impedance spectra of the surface of passivation coatings. The curve radius is the smallest when the current density is 20 A/dm² and highest when the current density is 40 A/dm². With the increase in the current density, the capacitive arc radius increases first and then decreases, indicating that the corrosion resistance of the coating also increases first and then decreases. At a current density of 40 A/dm², the composite coating exhibited the best corrosion resistance. As listed in Table 6, the charge transfer resistance R_p reaches a maximum value of 85.31 $\Omega \cdot \text{cm}^{-2}$ at a current density of 40 A/dm², i.e., 6.5 times higher than that at a current density of 20 A/dm². The higher the charge transfer resistance R_p , the greater the resistance of the charge transfer between the electrode and the solution [37] and the better the corrosion resistance—which also indicates that the composite coating exhibits the best corrosion resistance at a current density of 40 A/dm². This is consistent with the conclusions drawn from the polarization curve.

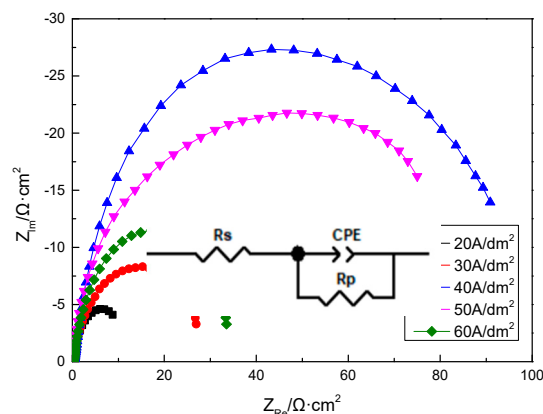


Figure 11. AC-impedance spectra of composite coating under different current density conditions.

Table 6. Equivalent circuit parameter values and error.

Current Density (A/dm ²)	R_s ($\Omega \cdot \text{cm}^{-2}$) (Error)	CPE-T (F·cm ⁻²) (Error)	CPE-P (Error)	R_p ($\Omega \cdot \text{cm}^{-2}$) (Error)
20	0.14877 (0.00311)	0.48417 (0.01609)	0.79896 (0.01491)	13.03 (1.2813)
30	0.22937 (0.00229)	0.02829 (0.00055)	0.76371 (0.00471)	26.70 (0.4169)
40	0.39187 (0.00827)	0.00779 (0.00015)	0.79891 (0.00435)	85.31 (1.2665)
50	0.20482 (0.00413)	0.00758 (0.00027)	0.81415 (0.00727)	63.41 (1.5542)
60	0.21519 (0.00469)	0.01905 (0.00069)	0.75339 (0.00795)	35.28 (1.0580)

3.4.3. Surface Morphology of Composite Coating after Corrosion

Figure 12 shows the surface morphologies of the N-P-ZrO₂-CeO₂ composite coating after corrosion, analyzed by SEM. When the current densities are 20 and 30 A/dm², many cracks, pits, bumps, and slice structures can be seen on the surface of the coatings. The surface is uneven, the surface quality after corrosion is poor, and many corrosion products appear on the surface defects. The analysis shows that the cell structure of the composite coating is not evident when the current density is low, and the boundary of the cell structure is complicated. The number of nanoparticles deposited in the composite

coating is small, and the fine-grain strengthening, and dispersion strengthening are weak, which increases the number of surface cracks of the composite coating. The corrosion process is concentrated at the boundary of the cell structure, on the surface defects, on the microcracks and at the gaps on the surface; this makes the composite coating to easily erode due to the corrosive media with strong penetration. When the current density is 40 A/dm², the surface of the coating is flat and clean, largely free of cracks and pits, and there are only a few corrosion pits with a size of $\leq 1 \mu\text{m}$. This is because the number of nanoparticles distributed in the coating is the highest at this time, the coating structure is uniform and dense, and the coating surface quality is good. The evenly distributed nanoparticles serve as strengthening phases in the coating, improving the chemical stability of the composite coating and extending the path of the corrosive medium into the composite coating. The corrosion pattern changes from pitting corrosion to uniform corrosion, making the composite coating to better withstand corrosion. Moreover, the embedding of ZrO₂ and CeO₂ nanoparticles led to the formation of a corrosion cell with Ni-P as the anode and nanoparticles as the cathode [38]. The formation of the corrosion cell effectively inhibited the corrosion process, promoting anodic polarization and making the corrosion uniform. When the current density is 50 A/dm², there are evident cracks and shedding on the surface of the composite coating, because of the increase in the internal force of the composite coating with increasing current density. When the current density is 60 A/dm², evident corrosion pits and holes appear on the surface of the composite coating, and the coating is broken and cracked. This is because the surface quality of the composite coating is poor, and there are many defects. During the corrosion process, the corrosion medium easily penetrates and diffuses into the composite coating, causing serious local corrosion.

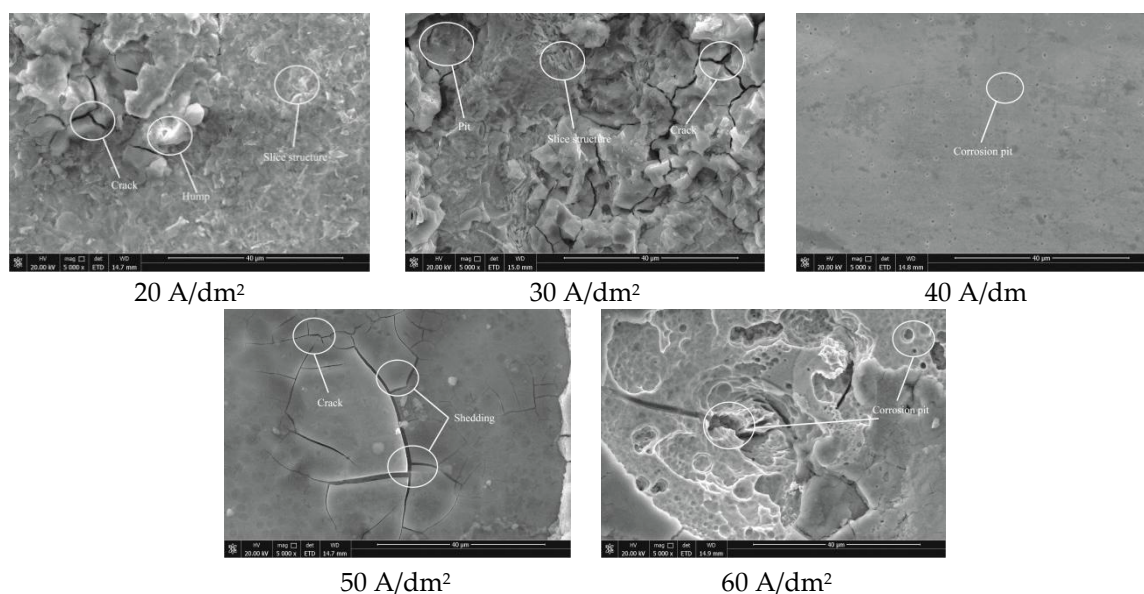


Figure 12. SEM images of surface micromorphology of Ni-P-ZrO₂-CeO₂ coatings after corrosion.

4. Conclusions

- The morphology of Ni-P-ZrO₂-CeO₂ composite coatings exhibited a typical cellular structure. With the increase in the current density, the surface flatness and surface quality of the composite coating increased first and then decreased. At a current density of 40 A/dm², the cell structure of the composite coating was uniform, the particle distribution was uniform, and the surface quality was the best.
- The composite coating was composed of a mixture of crystalline and amorphous phases. The grain size of the Ni (111) crystal plane tended to first decrease, and then increase with increasing current density. At a current density of 40 A/dm², the grain size reached a minimum of 6.2 nm. At this time, the effect of grain refinement was the most evident. When the current density was

40 A/dm², the contents of Zr and Ce in the composite coating were the maximum: 3.79% and 10.36%, respectively.

- The microhardness of Ni–P–ZrO₂–CeO₂ composite coating tended to first increase and then decrease with increasing current density. At a current density of 40 A/dm², the hardness of the composite coatings reached a maximum of 688.9 HV_{0.1}, which was approximately 12.5% higher than those prepared at a current density of 20 A/dm². At this time, the composite coating exhibited a dense structure and the highest hardness value.
- With the increase in the current density, the wear resistance of the Ni–P–ZrO₂–CeO₂ composite coatings tended to increase first and then decrease. At a current density of 40 A/dm², a large number of nanoparticles evenly distributed in the composite coating played the role of a “sliding ball.” To a certain extent, it made up for the pits and scratches left after the coating surface was damaged by abrasion and a “protective film” structure was formed on the surface, thereby improving the wear resistance.
- With the increase in the current density, the corrosion resistance tended to first increase and then decrease. At a current density of 40 A/dm², the corrosion current reached a minimum of 8.2501×10^{-5} A·cm⁻², and the corrosion potential reached a maximum of −0.45957 V. At this time, the capacitive arc radius was the largest, and the charge transfer resistance was the highest, indicating that the surface charge conduction resistance was the highest, and the coating exhibited the best corrosion resistance.

Author Contributions: Conceptualization, Z.S., M.S., and X.F.; methodology, Q.W. and Z.S.; software, Z.S. and J.L.; validation, X.F., M.S., and S.D.; formal analysis, Z.S.; investigation, Q.W., Z.S., and S.D.; resources, Z.S. and H.Z.; data curation, Z.S. and Q.W.; writing—original draft preparation, J.L. and Z.S.; writing—review and editing, J.L., Q.W.; visualization, Z.S. and X.F.; supervision, M.S., Z.S., and J.L.; project administration, Q.W. and X.F.; funding acquisition, Z.S., X.F., and M.S. All authors have read and agreed to the published version of the manuscript.

Funding: Financial support for this work was provided by the China Postdoctoral Science Foundation (Grant No. 2017M621665), the Postdoctoral Science Foundation of Jiangsu Province of China (Grant No. 2018K022A), National Natural Science Foundation of China (Grant No. 51605314), the Construction Plan of Innovation Team in Key Areas of Xinjiang Production and Construction Corps (Grant No. 2019CB006), the Plan of Major Science and Technology of Xinjiang Production and Construction Corps (Grant No. 2018AA008), the Supporting Plan for Regional Development and Innovation of the Division of Xinjiang Production and Construction Corps (Grant No. 2018BB014).

Conflicts of Interest: The authors declare no conflicts of interest.

References

1. Lin, L.B.; Dai, P.Q.; Lin, L.F.; Liao, Y.X. Corrosion characteristics of nanocrystalline Co-Ni-Fe deposits in 3.5% NaCl solution. *Rare Metal Mater. Eng.* **2012**, *41*, 851–856. (In Chinese)
2. Ding, W.Y.; He, X.C.; Xing, B.Y.; Zeng, K. Corrosion behavior and failure form of AA5052 aluminum alloy self-piercing riveted joint in periodic immersion environment. *Hot Working Technol.* **2018**, *47*, 1–4. (In Chinese)
3. Karimzadeha, A.; Aliofkhazraei, M.; Walsh, F.C. A review of electrodeposited Ni-Co alloy and composite coating: Microstructure, properties and applications. *Surf. Coat. Technol.* **2019**, *372*, 463–499. [\[CrossRef\]](#)
4. Tam, J.; Lau, J.C.F.; Erb, U. Thermally robust non-wetting Ni-PTFE electrodeposited nanocomposite. *Nanomaterials* **2018**, *9*, 2. [\[CrossRef\]](#) [\[PubMed\]](#)
5. Ding, X.L.; Hu, Z.F.; Jin, G.; Lyu, B.; Wang, X.H. Microstructure and properties of electro-brush plating Ni-graphene composite coating. *J. Mater. Eng.* **2018**, *46*, 110–117. (In Chinese)
6. Tahmasebpour, M.B.; Babaluo, A.A.; Aghjeh, M.K.R. Synthesis of zirconia nanopowders from various zirconium salts via polyacrylamide gel method. *J. Eur. Ceram. Soc.* **2008**, *28*, 773–778. [\[CrossRef\]](#)
7. Xue, Y.J.; Liu, H.B.; Lan, M.M.; Ku, X.C.; Li, J.X. High temperature oxidation resistance of Ni-CeO₂ nanocomposite coatings by pulse electrodeposition under ultrasound condition. *Trans. Nonferrous Met. Soc.* **2010**, *20*, 1599–1604. (In Chinese)
8. Schmidt, T.; Mennig, M.; Schmidt, H. New method for the preparation and stabilization of nanoparticulate t-ZrO₂ by a combined sol-gel and solvothermal process. *J. Am. Ceram. Soc.* **2007**, *90*, 1401–1405. [\[CrossRef\]](#)

9. Sheng, M.Q.; Weng, W.P.; Wang, Y.; Wu, Q.; Hou, S. Co-W/CeO₂ composite coatings for highly active electrocatalysis of hydrogen evolution reaction. *J. Alloys Compd.* **2018**, *743*, 682–690. [\[CrossRef\]](#)
10. Li, B.S.; Zhang, W.W.; Li, D.D. Synthesis and properties of a novel Ni-Co and Ni-Co/ZrO₂ composite coating by DC electrodeposition. *J. Alloys Compd.* **2020**, *821*, 153258. [\[CrossRef\]](#)
11. Laszczyńska, A.; Winiarski, J.; Szczygieł, B.; Szczygieł, I. Electrodeposition and characterization of Ni-Mo-ZrO₂ composite coatings. *Appl. Surf. Sci.* **2016**, *369*, 224–231. [\[CrossRef\]](#)
12. Li, J.S.; Xue, Y.J.; Lan, M.M.; Liu, Y.; Yu, Y.J. Effects of ultrasound on microstructures and properties of Ni-CeO₂ nanocomposite electroforming deposits. *Chin. J. Nonferr. Metal.* **2009**, *19*, 517–522.
13. Li, B.S.; Li, D.D.; Mei, T.Y.; Zhang, W. Fabrication and optimization of Ni-W/ZrO₂-CeO₂ composite coating for enhanced hardness and corrosion resistance. *Results Phys.* **2019**, *13*, 102375. [\[CrossRef\]](#)
14. Yang, B.; Zhang, P.; Wang, G.; Wang, A.; Chen, X.; Wei, S.; Xie, J. Effect of graphene oxide concentration in electrolyte on corrosion behavior of electrodeposited Zn–electrochemical reduction graphene composite coatings. *Coatings* **2019**, *9*, 758. [\[CrossRef\]](#)
15. Fu, X.; Ma, W.; Duan, S.; Wang, Q.; Lin, J. Electrochemical corrosion behavior of Ni-Fe-Co-P alloy coating containing nano-CeO₂ particles in NaCl solution. *Materials* **2019**, *12*, 2614. [\[CrossRef\]](#)
16. Wang, Y.; Ju, Y.; Wei, S.; Lu, W.; Yan, B.; Gao, W. Mechanical properties and microstructure of Au-Ni-TiO₂ nano-composite coatings. *Mater. Charact.* **2015**, *102*, 189–194. [\[CrossRef\]](#)
17. Guglielmi, N. Kinetics of the deposition of inert particles from electrolytic baths. *J. Electrochem. Soc.* **1972**, *119*, 1009–1012. [\[CrossRef\]](#)
18. Liu, Y.; Lu, G.L.; Liu, J.D.; Li, L. Electroplating n-ZrO₂/Ni composite coatings on AZ91D magnesium alloy and corrosion resistance. *Funct. Mater.* **2012**, *43*, 650–652, 656. (In Chinese)
19. Zhang, H.; Zhang, X.; Zhao, X.; Tang, Y.; Zuo, Y. Preparation of Ti-Zr-based conversion coating on 5052 aluminum alloy, and its corrosion resistance and antifouling performance. *Coatings* **2018**, *8*, 397. [\[CrossRef\]](#)
20. Zheng, Z.; Li, N.; Li, D.Y.; Meng, F.Y. Effect of CeO₂ on the property of Zn-Ni/CeO₂ composite coating. *Surf. Technol.* **2012**, *41*, 23–26. (In Chinese)
21. Beltowska-Lehman, E.; Indyka, P.; Bigos, A.; Szczerba, M.J.; Kot, M. Ni-W/ZrO₂ nanocomposites obtained by ultrasonic DC electrodeposition. *Mater. Des.* **2015**, *80*, 1–11. [\[CrossRef\]](#)
22. Walsh, F.C.; Low, C.T.J.; Bello, J.O. Influence of surfactants on electrodeposition of a Ni-nanoparticulate SiC composite coating. *Trans. IMF* **2015**, *93*, 147–156. [\[CrossRef\]](#)
23. Niazi, H.; Yari, S.; Golestani-Fard, F.; Shahmiri, M.; Wang, W.; Alfantazi, A.; Bayati, R. How deposition parameters affect corrosion behavior of TiO₂-Al₂O₃ nanocomposite coatings. *Appl. Surf. Sci.* **2015**, *335*, 1242–1252. [\[CrossRef\]](#)
24. Wang, W.; Hou, F.Y.; Guo, H.T. Relationship between dispersibility of ZrO₂ nanoparticles in Ni-ZrO₂ electroplated nanocomposite coatings and mechanical properties of nanocomposite coatings. *Trans. Nonferr. Metal Soc. China* **2004**, *14*, 186–189.
25. Liang, Z.P.; Wang, Y.Y.; Jin, H.; Zhou, X.Y.; Liu, X.L. Study on morphology and properties of Ni-Co/ZrO₂ composite coatings. *Rare Metals Cem. Carbides* **2018**, *46*, 59–63, 67. (In Chinese)
26. Aruna, S.T.; Bindu, C.N.; Ezhil, S.V.; Grips, V.W.; Rajam, K.S. Synthesis and properties of electrodeposited Ni/ceria nanocomposite coatings. *Surf. Coat. Technol.* **2006**, *200*, 6871–6880. [\[CrossRef\]](#)
27. Ao, Z.H.; Xue, Y.J.; Jiang, S.F.; Zhang, D.Y.; Li, X.H. Effects of different electrodeposition methods on corrosion resistance of Ni-ZrO₂ nanocomposite coatings. *Surf. Technol.* **2015**, *44*, 72–76. (In Chinese)
28. Xue, Y.J.; Si, D.H.; Liu, H.B.; Li, J.S.; Lan, M.M. Effects of electrodeposition methods on friction and wear properties of Ni-CeO₂ nanocomposite coatings. *Chin. J. Nonferr. Metal.* **2011**, *21*, 2157–2162. (In Chinese)
29. Ranganatha, S.; Venkatesha, T.V.; Vathsala, K. Development of high performance electroless Ni-P-HNT composite coating. *Appl. Surf. Sci.* **2012**, *263*, 149–156. [\[CrossRef\]](#)
30. Qiu, M.; Zhang, R.; Li, Y.C.; Pang, X.X. Effects of CeO₂ addition on tribological performance of MoS₂ based composite coatings. *J. Chin. Rare Earth Soc.* **2018**, *36*, 221–228. (In Chinese)
31. Bates, B.L.; Witman, J.C.; Zhang, Y. Electrolytic co-deposition of Ni-GrAlY composite coatings using different deposition configurations. *Mater. Manuf. Process.* **2016**, *31*, 1232–1237. [\[CrossRef\]](#)
32. Goto, Y.; Kamebuchi, Y.; Hagio, T.; Kamimoto, Y.; Ichino, R.; Bessho, T. Electrodeposition of copper/carbonous nanomaterial composite coatings for heat-dissipation materials. *Coatings* **2018**, *8*, 5. [\[CrossRef\]](#)

33. Yusuf, M.M.; Radwan, A.B.; Shakoor, R.A.; Awais, M.; Abdullah, A.M.; Montemor, M.F.; Kahraman, R. Synthesis and characterisation of Ni-B/Ni-P-CeO₂ duplex composite coatings. *J. Appl. Electrochem.* **2018**, *48*, 391–404. [[CrossRef](#)]
34. Anandan, C.; Bera, P. XPS studies on the interaction of CeO₂ with silicon in magnetron sputtered CeO₂ thin films on Si and Si₃N₄ substrates. *Appl. Surf. Sci.* **2013**, *283*, 297–303. [[CrossRef](#)]
35. Wan, B.; Li, H.X.; Zhou, H.F.; Yang, Q. Effect of indium sulfate on electrochemical behavior of nickel-diamond composite electrodeposition. *Electroplat. Finish.* **2016**, *35*, 1103–1106, 1147. (In Chinese)
36. Xu, Q.Y.; He, W.J. Research progress on rare earth in electroless Ni-P coating. *Surf. Technol.* **2011**, *40*, 92–96. (In Chinese)
37. Zhang, J.Y.; Yang, Q.J. Effects of RE-doped in the bath on nickel-base electroless deposit. *Surf. Technol.* **2012**, *41*, 44–46, 50. (In Chinese)
38. Lajevardi, S.A.; Shahrabi, T. Effects of pulse electrodeposition parameters on the peoperties of Ni-TiO₂ nanocomposite coatings. *Appl. Surf. Sci.* **2010**, *256*, 6775–6781. [[CrossRef](#)]



© 2020 by the authors. Licensee MDPI, Basel, Switzerland. This article is an open access article distributed under the terms and conditions of the Creative Commons Attribution (CC BY) license (<http://creativecommons.org/licenses/by/4.0/>).